Rapid Communications

Noncollinear antiferromagnetic Mn_3Sn films

A. Markou,[1,*] J. M. Taylor,[2] A. Kalache,[1] P. Werner,[2] S. S. P. Parkin,[2] and C. Felser[1,†]
[1]*Max Planck Institute for Chemical Physics of Solids, Nöthnitzer Str. 40, 01187 Dresden, Germany*
[2]*Max Planck Institute of Microstructure Physics, Weinberg 2, 06120 Halle, Germany*

(Received 12 February 2018; published 2 May 2018)

Noncollinear hexagonal antiferromagnets with almost zero net magnetization were recently shown to demonstrate giant anomalous Hall effect. Here, we present the structural and magnetic properties of noncollinear antiferromagnetic Mn_3Sn thin films heteroepitaxially grown on Y:ZrO_2 (111) substrates with a Ru underlayer. The Mn_3Sn films were crystallized in the hexagonal $D0_{19}$ structure with c-axis preferred (0001) crystal orientation. The Mn_3Sn films are discontinuous, forming large islands of approximately 400 nm in width, but are chemical homogeneous and characterized by near perfect heteroepitaxy. Furthermore, the thin films show weak ferromagnetism with an in-plane uncompensated magnetization of $M = 34$ kA/m and coercivity of $\mu_0 H_c = 4.0$ mT at room temperature. Additionally, the exchange bias effect was studied in Mn_3Sn/Py bilayers. Exchange bias fields up to $\mu_0 H_{EB} = 12.6$ mT can be achieved at 5 K. These results show Mn_3Sn films to be an attractive material for applications in antiferromagnetic spintronics.

DOI: 10.1103/PhysRevMaterials.2.051001

I. INTRODUCTION

Antiferromagnetic spintronics is a rapidly developing field that has received much attention in recent years and could represent the next advance in spintronic applications, as antiferromagnets show several advantages compared to the ferromagnets currently utilized. Antiferromagnets do not produce stray fields, are robust to external perturbations from magnetic fields, and show ultrafast spin dynamics and current-induced phenomena [1–6]. Among many different antiferromagnetic [7–9] or artificial antiferromagnetic materials [10,11], the noncollinear chiral antiferromagnets have attracted much interest, due to their remarkable structural, magnetic, and electrotransport properties. The trianglular spin structure of these compounds gives rise to a large anomalous Hall effect (AHE) [12,13], thermoelectric effect [14–16], magneto-optical Kerr effect [17,18], and spin Hall effect (SHE) [19]. Inspired by experimental work in Mn_3Ir [19], *ab initio* calculations confirmed large anisotropic anomalous Hall current and spin Hall current in these materials [20], while predicting that charge current is also spin polarized [21].

Hexagonal Mn_3Z (Z = Ga, Ge, and Sn) compounds are noncollinear antiferromagnets that crystallize in the $D0_{19}$ structure. Mn_3Sn and Mn_3Ge were theoretically predicted to show large AHE driven by nonvanishing Berry curvature [13], while band-structure calculations reveal that both compounds demonstrate a Weyl semimetal state with several Weyl points around the Fermi level [22,23]. In accordance with these theoretical calculations, single crystals of Mn_3Sn and Mn_3Ge were found to exhibit large AHE [24–26] and large anomalous Nernst effect [14,15], reaching the same order of magnitude as in ferromagnetic materials. These studies concern bulk single crystal, but to extend to spintronic devices thin films of these materials are required.

Up to now, the only report on hexagonal noncollinear antiferromagnetic thin films is from Mn_3Ga, as a bottom pinning antiferromagnet layer for magnetic tunnel junctions [27]. The Mn_3Ga film was (0001) oriented, showing low magnetization and large coercivity. The magnetic properties measured parallel and perpendicular to the film plane indicate that the net magnetization of the Mn_3Ga film was almost isotropic.

Mn_3Sn crystallizes in the hexagonal Mg_3Cd-type structure ($D0_{19}$), with space group $P6_3/mmc$ (No. 194) as shown in Fig. 1(a) and lattice constants of $a = b = 5.670$ Å, $c = 4.530$ Å. The Mn atoms form a kagome-type lattice in basal planes stacked along the c axis, where Sn atoms are located at the center of hexagons formed by Mn atoms. Mn_3Sn has a Néel temperature of $T_N = 420$ K. Neutron diffraction studies have demonstrated that a noncollinear triangular spin configuration of the Mn moments is obtained below T_N, where the neighboring moments are aligned at an angle of 120° [28,29], as shown in Fig. 1(b). Furthermore, Mn_3Sn shows weak ferromagnetism [30], owing to geometrical frustration of the Dzyaloskinskii-Moriya interaction (DMI) stabilized antiferromagnetic structure, which slightly cants spins toward in-plane easy axes.

In this work, we present the structural and magnetic properties of antiferromagnetic Mn_3Sn films with hexagonal structure and the results of exchange bias using these thin films. For this purpose, we performed systematic x-ray diffraction (XRD), transmission electron microscopy (TEM), and magnetic characterization of films heteroepitaxially grown on ZrO_2 substrates.

*anastasios.markou@cpfs.mpg.de
†claudia.felser@cpfs.mpg.de

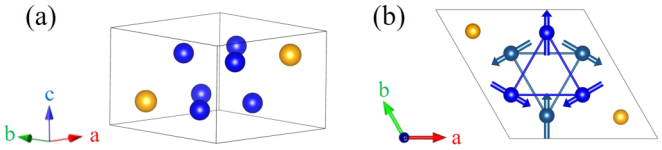

FIG. 1. (a) Crystal and (b) magnetic structure of Mn_3Sn, where the blue and orange spheres correspond to the Mn and Sn atoms, respectively.

II. EXPERIMENTAL DETAILS

Mn_3Sn films with thicknesses of 5–40 nm have been grown heteroepitaxially on single-crystal yttrium stabilized ZrO_2 (111) substrates with a 5 nm Ru underlayer. A BESTEC UHV magnetron sputtering system was used for the deposition of the films, with Mn (2″), Sn (2″), and Ru (2″) sources in confocal geometry. The target to substrate distance was 8″. Prior to deposition, the chamber was evacuated to a base pressure less than 2×10^{-8} mbar, while the process gas (Ar 5 N) pressure was 3×10^{-3} mbar. The total stack was Y:ZrO_2/Ru(5 nm)/Mn_3Sn(5–40 nm)/Al(2 nm). The Ru underlayer was deposited at a rate of 0.27 Å/s by applying 40 W dc power. The Mn_3Sn films were grown by cosputtering. The Mn was deposited at a rate of 0.48 Å/s by applying 55 W dc power and the Sn at a rate of 0.29 Å/s by applying 10 W dc power. The growth rates and the film thicknesses were determined by a quartz crystal microbalance and confirmed by using x-ray reflectivity measurements. The substrates were rotated during deposition, to ensure homogeneous growth. The Ru underlayer and the Mn_3Sn films were grown at 500 °C and then post-annealed *in situ* for an additional 10 min. In order to study the exchange bias effect, an additional stack was prepared of Y:ZrO_2/Ru(10 nm)/Mn_3Sn(40 or 20 nm)/Py(5 nm)/Al(2 nm), under the same conditions, with the Permalloy (Py = $Ni_{80}Fe_{20}$) film grown at room temperature (RT). All samples were capped at RT with a 2-nm-thick Al film to prevent oxidation.

Stoichiometry was estimated as $Mn_{74}Sn_{26}$ by energy-dispersive x-ray spectroscopy (EDXS) and verified by inductively coupled plasma optical emission spectrometry. XRD was measured with a PANalytical X'Pert^3 MRD diffractometer, using Cu Kα1 radiation ($\lambda = 1.5406$ Å). Conventional TEM, high-resolution TEM, and scanning transmission electron microscopy (STEM) were performed using a FEI Titan 80-300 microscope. For high-resolution STEM imaging, the high-angle annular dark-field technique (HAADF-STEM) was applied. Additionally, the Titan was equipped with EDXS for element mapping with high spatial resolution. Cross-section samples were prepared by focused ion beam milling. A protective C-Pt layer was deposited on the stack before starting the cross-section preparation. Magnetic measurements were carried out using a Quantum Design (MPMS 3 SQUID-VSM) magnetometer.

III. RESULTS AND DISCUSSION

A. Structural properties

Different XRD measurements, 2θ-ω scan, rocking curve (ω scan), and phi-scan, were performed to study the structure, the crystallinity, and the heteroepitaxial relationship between

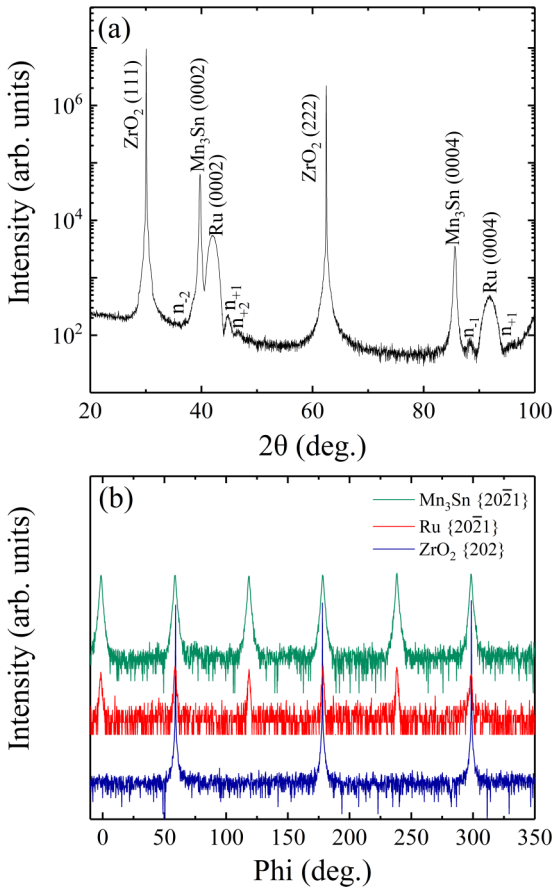

FIG. 2. (a) XRD pattern of the 40 nm Mn_3Sn film on 5 nm Ru underlayer. (b) Phi-scan patterns of the hexagonal {20$\bar{2}$1} planes from the Mn_3Sn film and Ru underlayer, and the cubic {202} planes from the ZrO_2 substrate.

the films and the substrate, respectively. The lattice mismatch between the substrate and the Ru underlayer is 4.44%, and between the Ru underlayer and the Mn_3Sn film is 5.26%, which allow the heteroepitaxial growth of *c*-axis oriented films. Figure 2(a) shows the XRD pattern of the 40 nm Mn_3Sn film. The (111) and (222) reflections from the Y:ZrO_2 substrate, and the (0002) and (0004) reflections from the hcp Ru were observed, suggesting that the Ru underlayer is (0001) oriented. The Ru main diffraction peaks are surrounded by Pendellösung fringes ($n_{\pm1}$, $n_{\pm2}$), which indicate a sharp interface between film and substrate and a high-crystalline quality along the *c* axis. Only the (0002) and (0004) reflections from the Mn_3Sn film were observed in XRD patterns, which demonstrates that the sample is crystallized in the hexagonal $D0_{19}$ structure with (0001) preferred orientation and the *c* axis normal to the film plane.

Phi-scan patterns of the hexagonal {20$\bar{2}$1} planes from the Mn_3Sn film and Ru underlayer, and the cubic {202} planes from the Y:ZrO_2 substrate, are depicted in Fig. 2(b). The six reflections of the Mn_3Sn film and Ru underlayer show sixfold symmetry with 60° intervals, suggesting hexagonal single-crystalline epilayers with well-defined in-plane orientation. The three different sets of lattice planes occur at the same azimuthal angle ϕ, which indicates that the

TABLE I. Lattice constants a and c, and the FWHM of the (0002) rocking curve profile, for Mn_3Sn thin films with different thicknesses.

Thickness (nm)	a (Å) ±0.002 Å	c (Å) ±0.002 Å	FWHM (deg.)
5	5.689	4.537	0.780
10	5.691	4.534	0.759
20	5.694	4.532	0.748
40	5.695	4.532	0.566

unit cells of the Mn_3Sn film and Ru underlayer are well aligned in the basal planes of the Y:ZrO_2 substrate. The crystallographic orientation relationship is thus determined as Y:$ZrO_2(111)[1\bar{1}0]\|Ru(0001)[11\bar{2}0]\|Mn_3Sn(0001)[11\bar{2}0]$.

The measured lattice parameters a and c, and the full width at half maximum (FWHM) of the (0002) out-of-plane rocking curve are summarized in Table I. The lattice parameter c is deduced from the (0002) and (0004) reflections of the out-of-plane XRD patterns, while the lattice parameter a is estimated from the in-plane $(20\bar{2}1)$ reflection. For the measurement of the in-plane reflection, the detector was used in 0D scanning mode to create a 2D $2\theta/\omega$-χ scan map, in which the $(20\bar{2}1)$ reflection appears as a peak with Gaussian shape. The $(20\bar{2}1)$ reflection was chosen because its intensity is the strongest, thus making investigation of the reflection possible even for 5-nm-thick films. The c and a lattice parameters are very close to the bulk values. As the film thickness is decreased, a decreases, while c increases. This dependence of the lattice constants with decreasing film thickness can be explained in terms of inner strain, due to lattice mismatch and different thermal expansion coefficients between the epilayers and the substrate. The crystal quality of the Mn_3Sn films was evaluated from the FWHM values of rocking curves measured around (0002) reflections. The high intensity of the curve combined with small FWHM $\approx 0.566^\circ$ suggests that the 40-nm-thick sample shows high-crystalline quality with low mosaicity (see Supplemental Material [31]). At lower thicknesses the FWHM is slightly higher, owing to the limited film thickness and/or presence of defects.

B. TEM analysis

TEM was performed to evaluate the film quality on the nanoscale. A cross-section high-resolution HAADF-STEM image of the 40-nm-thick Mn_3Sn film is represented in Fig. 3(a). The crystal lattice of the Mn_3Sn film is characterized by nearly perfect heteroepitaxy. Close to the interface between the Mn_3Sn film and the Ru underlayer, a small amount of planar defects are observed. They have the character of stacking faults within the stacking sequence of the (0001) planes along the [0001] growth direction. An example is shown in Fig. 3(a), where stacking faults are indicated by dashed lines. We attribute these planar faults to strain relaxation in the Mn_3Sn lattice, as similarly observed in other heteroepitaxial systems [32,33]. Moving away from the interface, further epitaxial growth of the Mn_3Sn layer proceeds along the [0001] direction without defects. The inset of Fig. 3(a) illustrates the scheme of the Mn_3Sn crystal lattice according to the chosen $\langle 01\bar{1}0\rangle$ orientation for the TEM observation. The large orange spheres

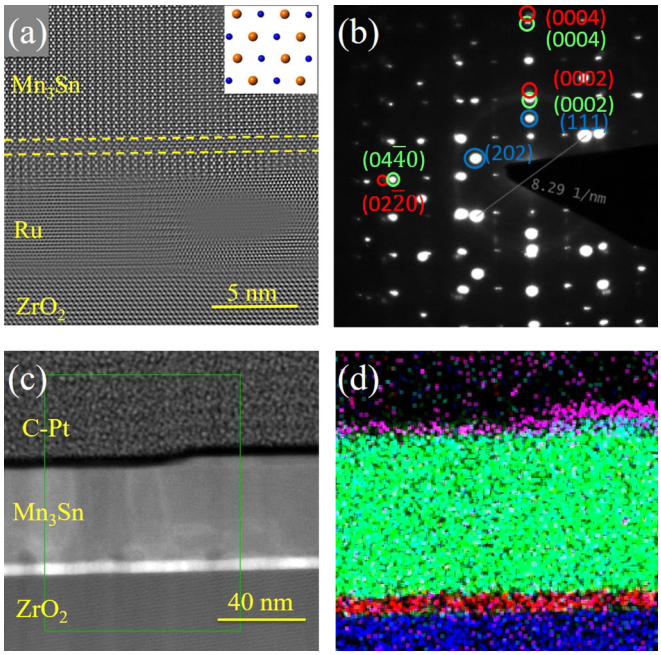

FIG. 3. (a) Cross-section HRSTEM image of the 40 nm Mn_3Sn film grown on Y:ZrO_2 substrate with a 5 nm Ru underlayer. The inset illustrates the scheme of the Mn_3Sn crystal lattice in the $\langle 01\bar{1}0\rangle$ direction, where the large orange spheres and the small blue spheres correspond to the Sn and Mn atoms, respectively. (b) SAED pattern showing the diffraction spots from Mn_3Sn (green open circles), Ru (red open circles), and Y:ZrO_2 (blue open circles). (c) Cross-section HAADF-STEM image, where the green box denotes the area where chemical mapping was performed. (d) Elemental mapping of Zr (blue), Ru (red), Mn (green), Sn (light blue), and Al (purple).

and the smaller blue spheres correspond to the Sn and Mn atoms, respectively. In the HAADF-STEM image the lattice of the Ru underlayer is locally blurred. This can be attributed to local strains and a misalignment of the crystal lattice due to strained-induced mosaicity. Furthermore, the TEM analysis reveals that the Mn_3Sn film is discontinuous, forming large islands of approximately 400 nm in width (see Supplemental Material). The growth of islands can be attributed to the large lattice mismatch between the Ru underlayer and Mn_3Sn film, which is 5.26%. Furthermore, the kinetic conditions (i.e., growth rate, temperature, and atomic mobility) during thin-film deposition may affect the morphology of the films, similar to the case of Mn_3Ga [34].

The selected area electron diffraction (SAED) pattern of the same sample is depicted in Fig. 3(b), where the electron beam is parallel to the $\langle 11\bar{2}0\rangle$ zone axis of the epilayers. The blue, red, and green open circles correspond to the diffraction spots from the substrate, the Ru underlayer, and the Mn_3Sn film, respectively. The three different sets of diffraction spots are aligned, confirming the coherent heteroepitaxial growth of the epilayers on the substrate. The indexed SAED pattern reveals that the Mn_3Sn film is crystallized in the hexagonal $D0_{19}$ structure. The lattice constants were determined to be $a = 5.676$ Å and $c = 4.495$ Å, which are in a good agreement with the XRD measurements. The small difference can be attributed to the larger measurement error result-

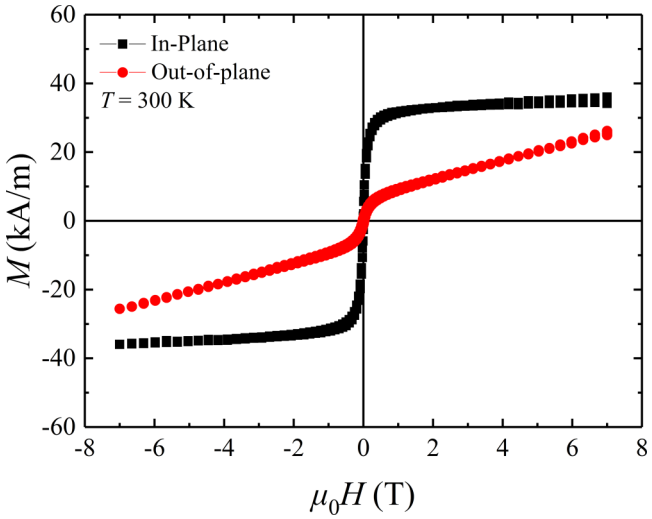

FIG. 4. In-plane and out-of-plane magnetization hysteresis loops of the 40 nm Mn_3Sn film.

ing from the analysis of local restricted electron diffraction patterns.

The element distribution within the Mn_3Sn films was analyzed by EDXS element mapping in the HAADF mode. An example is shown in Figs. 3(c) and 3(d). The green box in the HAADF image [Fig. 3(c)] indicates the area where the elemental analysis was performed. The spatial distribution of the count rate intensity for Mn, Sn, Ru, and Zr elements are represented with different colors in Fig. 3(d). Mn and Sn were detected at exactly the same sample regions, therefore confirming the homogeneity of the Mn_3Sn film. Due to the sharp interface between the Ru and Mn EDXS signals, we conclude that intermixing between the Mn_3Sn film and Ru underlayer does not occur.

C. Magnetic properties and exchange bias

Typical in-plane and out-of-plane magnetization hysteresis loops for the 40 nm Mn_3Sn film measured at 300 K are shown in Fig. 4. The Mn_3Sn film shows small spontaneous magnetization in plane. This uncompensated moment in otherwise noncollinear antiferromagnetic Mn_3Sn has been explained experimentally [28,30] and theoretically [35], due to geometric frustration of the Mn moments leading to canting in the *a*-*b* plane. Even though the Mn moments are expected to lie only in the *a*-*b* plane, a smaller additional moment is observed out of plane, indicating that Mn moments are tilted slightly toward the *c* axis, similar to bulk Mn_3Ge [25]. The weak ferromagnetism in this class of materials is useful, as it allows control of their transport properties, since a small external field can switch the moment orientation of the chiral spin structure.

In contrast with previously reported Mn_3Ga films, which show isotropic uncompensated magnetization in plane and out of plane accompanied by large coercivity ($\mu_0 H_c > 3$ T) [27], these Mn_3Sn films are anisotropic. The 40 nm film has an in-plane uncompensated moment of $M = 34$ kA/m and coercivity of $\mu_0 H_c = 4.0$ mT, while for a 20 nm film the magnetic properties are similar with an uncompensated

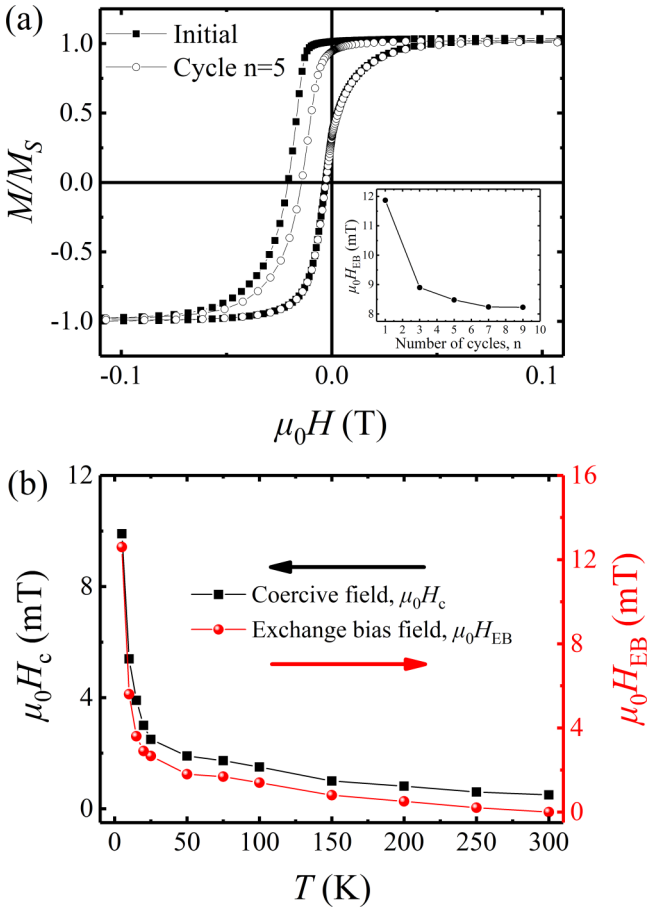

FIG. 5. (a) Initial (solid symbols) and trained (open symbols) in-plane magnetization hysteresis loops of the Mn_3Sn (40 nm)/Py (5 nm) bilayer at 5 K after 1 T FC. (b) Temperature dependence of exchange bias and coercive fields during field cooling.

moment of $M = 37$ kA/m and coercivity of $\mu_0 H_c = 3.8$ mT (see Supplemental Material). The in-plane uncompensated moment of the 40 nm film corresponds to $0.21\mu_B$/f.u. which is one order of magnitude larger than similar bulk single crystals [24–26]. The structure of bulk Mn_3Sn is stable in excess of Mn, which randomly occupies the Sn site, but in thin films it is stable even with less Mn (Mn:Sn ~74:26 at.%). We therefore propose that the larger magnetization observed in films compared to bulk can be attributed to additional uncompensated moments arising from disorder effects. The disorder is caused due to the excess of Sn randomly occupying Mn sites or due to Mn vacancies, as well as a possible slight antisite disorder with Sn/Mn exchanging their positions. Furthermore, the DMI, which is responsible for the triangular spin configuration, can produce only an in-plane moment, since the D_{ij} vector has to lie along the *c* axis. Thus the smaller out-of-plane moment observed in Fig. 4 indicates a small disruption to the expected anisotropy that tilts the Mn moments slightly toward the *c* axis. This shows that the excess of Sn on Mn sites or vacancies can cause a disorder in the triangular spin configuration, which in turn affects the magnetization through an increase of uncompensated moment. In addition, surface or bulk defects, lattice strain, and grain boundaries may introduce further uncompensated moment contributions.

Exchange bias (EB) results from interfacial exchange interactions between coupled antiferromagnetic and ferromagnetic (AFM/FM) systems [36]. EB is characterized by a shift in the magnetization hysteresis loop of the FM along the applied field axis, called the exchange bias field ($\mu_0 H_{EB}$), accompanied by a coercivity ($\mu_0 H_c$) enhancement. This phenomenon arises below a certain characteristic temperature of the AFM/FM system, known as the blocking temperature (T_B). EB is utilized to pin the magnetization of a FM layer in a desired direction in spintronic devices such as spin valves [37] and magnetic random-access memories [38].

The initial in-plane normalized magnetization hysteresis curve (solid symbols) of the Mn_3Sn (40 nm)/Py (5 nm) bilayer measured at 5 K after field cooling (FC) from 400 K under a 1 T in-plane magnetic field is depicted in Fig. 5(a). After FC the measured hysteresis loop is shifted along the negative direction of the applied field axis, and also vertically by +15 kA/m. The vertical loop shift indicates the presence of uncompensated pinned interfacial spins [39,40]. After correcting for the vertical shift, values of $\mu_0 H_c = 10.0$ mT and $\mu_0 H_{EB} = 12.6$ mT are determined. These results suggest the observed EB is mediated by a layer of uncompensated spins induced in Mn_3Sn at the interface with Py, a fraction of which are pinned (demonstrated by the vertical hysteresis loop shift) due to strong exchange coupling to the bulk Mn_3Sn antiferromagnetic order and thus inducing unidirectional anisotropy in the Py film. Following a number of hysteresis loop measurements, as shown in Fig. 5(a) (open symbols), a training effect of this exchange bias is observed. After five repeat cycles, we obtain consistent values of $\mu_0 H_{EB} = 8.0$ mT [inset of Fig. 5(a)]. This training effect can be attributed to a relaxation of uncompensated interfacial moments during field cycling, in turn lessening exchange bias. In addition, the exchange bias field is reversible when field cooled under a negative applied field, but otherwise found to be independent of cooling field strength (see Supplemental Material).

The temperature dependence of $\mu_0 H_c$ and $\mu_0 H_{EB}$ for the Mn_3Sn (40 nm)/Py (5 nm) bilayer is shown in Fig. 5(b). Each data point represents the displacement in the $M(H)$ loop measured after the bilayer was cooled from 400 K to different temperatures under a 1 T in-plane magnetic field. As the bilayer passes through its characteristic T_B, increasing exchange interactions act to pin the magnetization of Py. A rapid increase in both $\mu_0 H_c$ and $\mu_0 H_{EB}$ below 50 K indicates the onset of exchange coupling, allowing us to place the blocking temperature of a 40-nm-thick Mn_3Sn film in this range (see Supplemental Material).

IV. CONCLUSIONS

In summary, we have studied the structural and magnetic properties of Mn_3Sn films heteroepitaxially grown on Y:ZrO_2 (111) substrates with a 5 nm Ru underlayer. The films were crystallized in the hexagonal $D0_{19}$ structure with (0001) preferred orientation. TEM analysis reveals that the Mn_3Sn films, although discontinuous, are chemically homogeneous and characterized by near perfect heteroepitaxy. Magnetic measurements show weak anisotropic ferromagnetism in the films. The weak ferromagnetism in this class of materials allows control of their electrical transport properties, since a small external field can switch the moment orientation of the chiral spin structure. Furthermore, we have studied the exchange bias of Mn_3Sn/Py bilayers. Exchange bias fields up to $\mu_0 H_{EB} = 12.6$ mT are achieved at 5 K. Such exchange biased heterostructures open up the possibility of further interesting study investigating the spin-orbit torque produced by Mn_3Sn, similar to Mn_3Ir/Py [19], following predictions of a large SHE [20] and spin-polarized current [21]. Our results show that Mn_3Sn is an attractive material to study novel phenomena which may have a major impact in antiferromagnetic spintronic applications.

ACKNOWLEDGMENT

This work has been funded by EU FET Open RIA Grant No. 766566.

[1] E. V. Gomonay and V. M. Loktev, Low Temp. Phys. **40**, 17 (2014).
[2] T. Jungwirth, X. Marti, P. Wadley, and J. Wunderlich, Nat. Nanotechnol. **11**, 231 (2016).
[3] A. H. MacDonald and M. Tsoi, Philos. Trans. R. Soc. A **369**, 3098 (2011).
[4] J. Železný, H. Gao, K. Výborný, J. Zemen, J. Mašek, A. Manchon, J. Wunderlich, J. Sinova, and T. Jungwirth, Phys. Rev. Lett. **113**, 157201 (2014).
[5] A. S. Núñez, R. A. Duine, P. Haney, and A. H. MacDonald, Phys. Rev. B **73**, 214426 (2006).
[6] H. V. Gomonay and V. M. Loktev, Phys. Rev. B **81**, 144427 (2010).
[7] P. Borisov, A. Hochstrat, X. Chen, W. Kleemann, and C. Binek, Phys. Rev. Lett. **94**, 117203 (2005).
[8] A. B. Shick, S. Khmelevskyi, O. N. Mryasov, J. Wunderlich, and T. Jungwirth, Phys. Rev. B **81**, 212409 (2010).
[9] P. Wadley, V. Novák, R. P. Campion, C. Rinaldi, X. Martí, H. Reichlová, J. Zelezný, J. Gazquez, M. A. Roldan, M. Varela, D. Khalyavin, S. Langridge, D. Kriegner, F. Máca, J. Masek, R. Bertacco, V. Holý, A. W. Rushforth, K. W. Edmonds, B. L. Gallagher, C. T. Foxon, J. Wunderlich, and T. Jungwirth, Nat. Commun. **4**, 2322 (2013).
[10] S. S. P. Parkin, N. More, and K. P. Roche, Phys. Rev. Lett. **64**, 2304 (1990).
[11] P. J. H. Bloemen, H. W. van Kesteren, H. J. M. Swagten, and W. J. M. de Jonge, Phys. Rev. B **50**, 13505 (1994).
[12] H. Chen, Q. Niu, and A. H. MacDonald, Phys. Rev. Lett. **112**, 017205 (2014).
[13] J. Kübler and C. Felser, Europhys. Lett. **108**, 67001 (2014).
[14] M. Ikhlas, T. Tomita, T. Koretsune, M.-T. Suzuki, D. Nishio-Hamane, R. Arita, Y. Otani, and S. Nakatsuji, Nat. Phys. **13**, 1085 (2017).
[15] X. Li, L. Xu, L. Ding, J. Wang, M. Shen, X. Lu, Z. Zhu, and K. Behnia, Phys. Rev. Lett. **119**, 056601 (2017).
[16] H. Narita, M. Ikhlas, M. Kimata, A. A. Nugroho, S. Nakatsuji, and Y. Otani, Appl. Phys. Lett. **111**, 202404 (2017).
[17] W. Feng, G.-Y. Guo, J. Zhou, Y. Yao, and Q. Niu, Phys. Rev. B **92**, 144426 (2015).

[18] T. Higo, H. Man, D. B. Gopman, L. Wu, T. Koretsune, O. M. J. van 't Erve, Y. P. Kabanov, D. Rees, Y. Li, M.-T. Suzuki, S. Patankar, M. Ikhlas, C. L. Chien, R. Arita, R. D. Shull, J. Orenstein, and S. Nakatsuji, Nat. Photon. **12**, 73 (2018).
[19] W. Zhang, W. Han, S.-H. Yang, Y. Sun, Y. Zhang, B. Yan, and S. S. P. Parkin, Sci. Adv. **2**, e1600759 (2016).
[20] Y. Zhang, Y. Sun, H. Yang, J. Železný, S. P. P. Parkin, C. Felser, and B. Yan, Phys. Rev. B **95**, 075128 (2017).
[21] J. Železný, Y. Zhang, C. Felser, and B. Yan, Phys. Rev. Lett. **119**, 187204 (2017).
[22] H. Yang, Y. Sun, Y. Zhang, W.-J. Shi, S. S. P. Parkin, and B. Yan, New J. Phys. **19**, 015008 (2017).
[23] J. Kübler and C. Felser, Europhys. Lett. **120**, 47002 (2018).
[24] S. Nakatsuji, N. Kiyohara, and T. Higo, Nature (London) **527**, 212 (2015).
[25] A. K. Nayak, J. E. Fischer, Y. Sun, B. Yan, J. Karel, A. C. Komarek, C. Shekhar, N. Kumar, W. Schnelle, J. Kübler, C. Felser, and S. S. P. Parkin, Sci. Adv. **2**, e1501870 (2016).
[26] N. Kiyohara, T. Tomita, and S. Nakatsuji, Phys. Rev. Appl. **5**, 064009 (2016).
[27] H. Kurt, K. Rode, H. Tokuc, P. Stamenov, M. Venkatesan, and J. M. D. Coey, Appl. Phys. Lett. **101**, 232402 (2012).
[28] T. Nagamiya, S. Tomiyoshi, and Y. Yamaguchi, Solid State Commun. **42**, 385 (1982).
[29] S. Tomiyoshi, J. Phys. Soc. Jpn. **51**, 803 (1982).
[30] S. Tomiyoshi and Y. Yamaguchi, J. Phys. Soc. Jpn. **51**, 2478 (1982).
[31] See Supplemental Material at http://link.aps.org/supplemental/10.1103/PhysRevMaterials.2.051001 for further details on experimental measurements of the Mn_3Sn films.
[32] K. Aoyagi, Y. Kodama, T. Kiguchi, Y. Ehara, H. Funakubo, and T. J. Konno, Mater. Sci. Eng. B **177**, 528 (2012).
[33] C. H. Hsiao, Y. D. Yao, S. C. Lo, H. W. Chang, and C. H. Ouyang, Appl. Phys. Lett. **107**, 142407 (2015).
[34] C. L. Zha, R. K. Dumas, J. W. Lau, S. M. Mohseni, S. R. Sani, I. V. Golosovsky, Å. F. Monsen, J. Nogués, and J. Åkerman, J. Appl. Phys. **110**, 093902 (2011).
[35] L. M. Sandratskii and J. Kübler, Phys. Rev. Lett. **76**, 4963 (1996).
[36] J. Nogués and I. K. Schuller, J. Magn. Magn. Mater. **192**, 203 (1999).
[37] B. Dieny, V. S. Speriosu, S. S. P. Parkin, B. A. Gurney, D. R. Wilhoit, and D. Mauri, Phys. Rev. B **43**, 1297 (1991).
[38] S. S. P. Parkin, K. P. Roche, M. G. Samant, P. M. Rice, R. B. Beyers, R. E. Scheuerlein, E. J. O'Sullivan, S. L. Brown, J. Bucchigano, D. W. Abraham, Y. Lu, M. Rooks, P. L. Trouilloud, R. A. Wanner, and W. J. Gallagher, J. Appl. Phys. **85**, 5828 (1999).
[39] H. Ohldag, A. Scholl, F. Nolting, E. Arenholz, S. Maat, A. T. Young, M. Carey, and J. Stöhr, Phys. Rev. Lett. **91**, 017203 (2003).
[40] P. Kappenberger, S. Martin, Y. Pellmont, H. J. Hug, J. B. Kortright, O. Hellwig, and E. E. Fullerton, Phys. Rev. Lett. **91**, 267202 (2003).